

A Near-Inertial Internal Wave Spectrum for the Sargasso Sea in Late Summer

E. A. D'ASARO

Applied Physics Laboratory, University of Washington, Seattle, WA 98105

HENRY PERKINS

Naval Ocean Research and Development Activity, NSTL Station, MI 39529

(Manuscript received 8 August 1983, in final form 3 January 1984)

ABSTRACT

Independent estimates of the frequency-wavenumber spectrum of near-inertial internal waves for the Sargasso Sea in late summer were made using 8 time series of horizontal velocity from a single moored vertical array and 58 vertical profiles of horizontal velocity from a horizontal array of expendable velocity profilers. The profiler data were analyzed to produce an internal wave frequency-wavenumber spectrum with sufficient resolution to resolve the details of the inertial peak and compute the vertical energy flux. Comparison with the lower resolution spectrum from the moored array shows qualitative agreement; the differences are most likely due to biases in both techniques and to intermittency of the internal wave field.

These data reveal a marked asymmetry of the near-inertial internal wave field, with a net downward energy flux of $0.12 \pm 0.12 \text{ ergs cm}^{-2} \text{ s}^{-1}$. The downward propagating waves have more energy, a larger horizontal scale and a lower frequency than the upward propagating waves. The magnitude of the downward energy flux is comparable to the net input of energy into surface inertial currents, confirming the likely importance of the wind as an energy source for near-inertial internal waves.

1. Introduction

The "universal" internal wave spectra, which so successfully summarize deep-ocean internal wave measurements, fail to describe the observations near the inertial frequency (Garrett and Munk, 1979; Gregg and Briscoe, 1979; Fu, 1981). This is no mean failing, as a large fraction of the total internal wave energy is near-inertial. Numerous observations of wind-generated, inertial oscillations in the surface-mixed layer (Pollard and Millard, 1970; Pollard, 1980; Weller, 1982), coupled with observations of excess energy in downward propagating, near-inertial internal waves (Leaman and Sanford, 1975; Käse and Clark, 1978; Müller *et al.*, 1978), strongly suggest that much of the energy in near-inertial waves is wind-generated. Calculations of nonlinear, wave-wave interaction indicate that near-inertial waves are only weakly nonlinear (McComas and Müller, 1981) and that they should, unlike the "universal," highly nonlinear part of the wave field, reflect the distribution of their sources and sinks.

This paper will describe the properties of the near-inertial wave field in the upper kilometer of the Sargasso Sea in late summer using both a space-time array of horizontal velocity profiles and a vertical array of current meters. A frequency-wavenumber spectrum will be constructed using each data set. The comparison of these two independent spectra will illustrate the

strengths and weaknesses of both measurement techniques and, in particular, will demonstrate the power of the velocity profiling measurements to resolve internal waves with frequencies very close to the inertial frequency.

The vertical energy flux in a field of internal waves can be estimated by taking the product of the wave energy density and vertical group velocity and summing over all the waves. For a single, linear internal wave of the form $e^{i(kx+ly+\beta z-\sigma t)}$ (z positive upward), the hydrostatic dispersion relation relating horizontal wavenumber $\alpha^2 = k^2 + l^2$, vertical wavenumber β and frequency σ is

$$\sigma^2 - f^2 = \frac{\alpha^2 N^2}{\beta^2} \quad (1)$$

for Väisälä and inertial frequencies N and f (Garrett and Munk, 1979). Note that for a fixed vertical wavenumber β , the horizontal scale of the wave $1/\alpha$ becomes very large as σ approaches f . The vertical group velocity is

$$C_g = -\frac{N^2}{\sigma} \frac{\alpha^2}{\beta^3} \quad (2a)$$

or

$$C_g = -\frac{\sigma^2 - f^2}{\sigma \beta} \quad (2b)$$

If a time series of vertical profiles (or a densely instrumented mooring) is available, the group velocity

can be estimated using (2b). Typically, the peak of the internal wave spectrum is within 10% of f (Fu, 1981), so the time series must be at least several months long to estimate $\sigma^2 - f^2$, and thus C_g , accurately. Leaman's (1976) estimate of internal wave energy flux uses this approach. The major inaccuracy in his estimate results from the shortness of the available time series. If, rather, a spatial pattern of vertical profiles is made, the group velocity can be estimated using (2a) which substitutes spatial information for time information using the dispersion relation (1). The frequency spectrum of waves very near the inertial frequency can be obtained by measuring over large spatial scales rather than long times assuming, of course, internal wave dynamics. A wave with $\sigma = 1.01 f$, for example, has twice the scale of a wave with $\sigma = 1.04 f$. Such a difference is easily resolved with a spatial array (as will be demonstrated later). If, as seems likely, the sources for near-inertial internal waves are localized in space and time, a spatial survey that can be rapidly executed is well adapted to measuring the wave flux out of these source regions.

The velocity profile and current meter data are described in Sections 2 and 3, respectively. The wave-number-frequency spectra computed using each data set are described in Sections 4 and 5. The profiler and current meter results are compared in Section 6. Much of the wave field appears to be surface forced, as discussed in Section 7. Conclusions and further discussion occur in Sections 8 and 9, respectively. Further details of the profiler and current meter analysis are described in the Appendices.

2. Velocity profile data

Velocity profiles for this research were obtained using the Expendable Current Profiler (XCP; Sanford *et al.*, 1982). This is an expendable version of the electromagnetic profiler discussed by Sanford *et al.* (1978). This instrument uses electromagnetic induction in the earth's magnetic field to measure the horizontal vector velocity in the upper 800 m of the ocean to within a depth-independent constant. For this experiment the constant is set by assuming a zero vertical mean profile. Intercomparisons with other profilers suggest an rms error of 1 cm s^{-1} (Sanford *et al.*, 1982). The instrument depth at any time is computed from the time since launch using a standard time-variable fall speed. The resulting depth is accurate to 4 m, rms, averaged over the profile. This is comparable to the depth error for XBTs (Seaver and Kuleshov, 1982). In this data set, data within the upper 100 m are contaminated by the ship's electric field and are excluded from the analysis.

The XCPs were launched from the USNS *Kane* as part of the HYDRO-79 observations in the Sargasso Sea during September 1979 (Perkins, 1980). Ninety-two profiles were taken. An L-shaped sampling pattern was repeated three times on each of 2 days in the vicinity of a moored current-meter string (Fig. 1a). For the profiler analysis, only the low-frequency current-

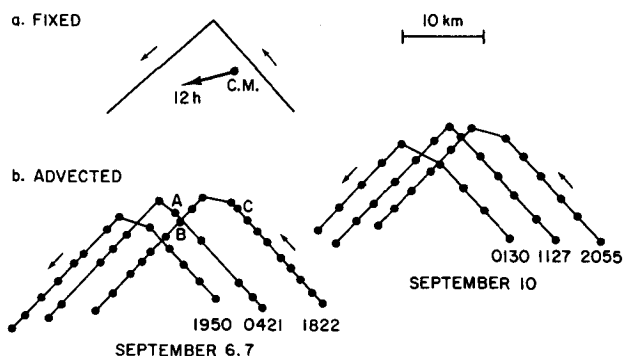


FIG. 1. (a) Sampling pattern of XCPs relative to mooring. Arrow shows 12 h displacement of water from current meters. (b) XCP profile positions in the advected coordinate system. Profiles A and C have the same geographical positions; profiles A and B have nearly the same advected positions.

meter velocities are important. Mean currents during the experiment were roughly 13 cm s^{-1} to the west-southwest (Fig. 1b) with time-mean velocity differences of less than 2 cm s^{-1} across the XCP depth range. The XBT and AXBT surveys showed no evidence of strong mesoscale eddies in the experimental area (Perkins, 1980).

Several distinctive features are apparent in the subset of profiles shown in Fig. 2a. A broad range of scales in both the vertical and horizontal is apparent. The velocity vector rotates dominantly in a clockwise direction with depth. Comparison of profiles taken at different times in roughly the same location indicates that the velocity vector rotates dominantly in a clockwise direction with time. These two features are typical of velocity profiles taken in the Sargasso Sea (Sanford, 1975). They suggest a wave field dominated by downward propagating near-inertial waves (Leaman, 1976).

This survey represents neither a pure spatial map nor a time series. For the near-inertial waves, however, a pure spatial survey can be approximated by assuming the profiles rotate clockwise with time, and back-rotating each to a common reference time. The horizontal scales of these "rotated" profiles (Fig. 2b) are very similar to those of the raw profiles (Fig. 2a), reflecting the high speed of the ship relative to the phase velocity of the dominant waves.

The measured velocity field is dominated by a few features. Assuming that these obey internal wave dynamics, their energy flux can be estimated. Consider, for example, the feature at 500 m and -5 km which has rough vertical and horizontal scales of 125 m and 25 km and an rms amplitude of 3 cm s^{-1} . Using (1) this yields a frequency of $\sigma/f = 1.03$ for $N/f = 50$, a vertical group velocity of roughly 50 m per day and a flux of $0.45 \text{ ergs cm}^{-2} \text{ s}^{-1}$. The XCP analysis performed as follows is similar but statistical and more rigorous.

Internal waves are best observed not in a fixed coordinate system, but in an advected coordinate system

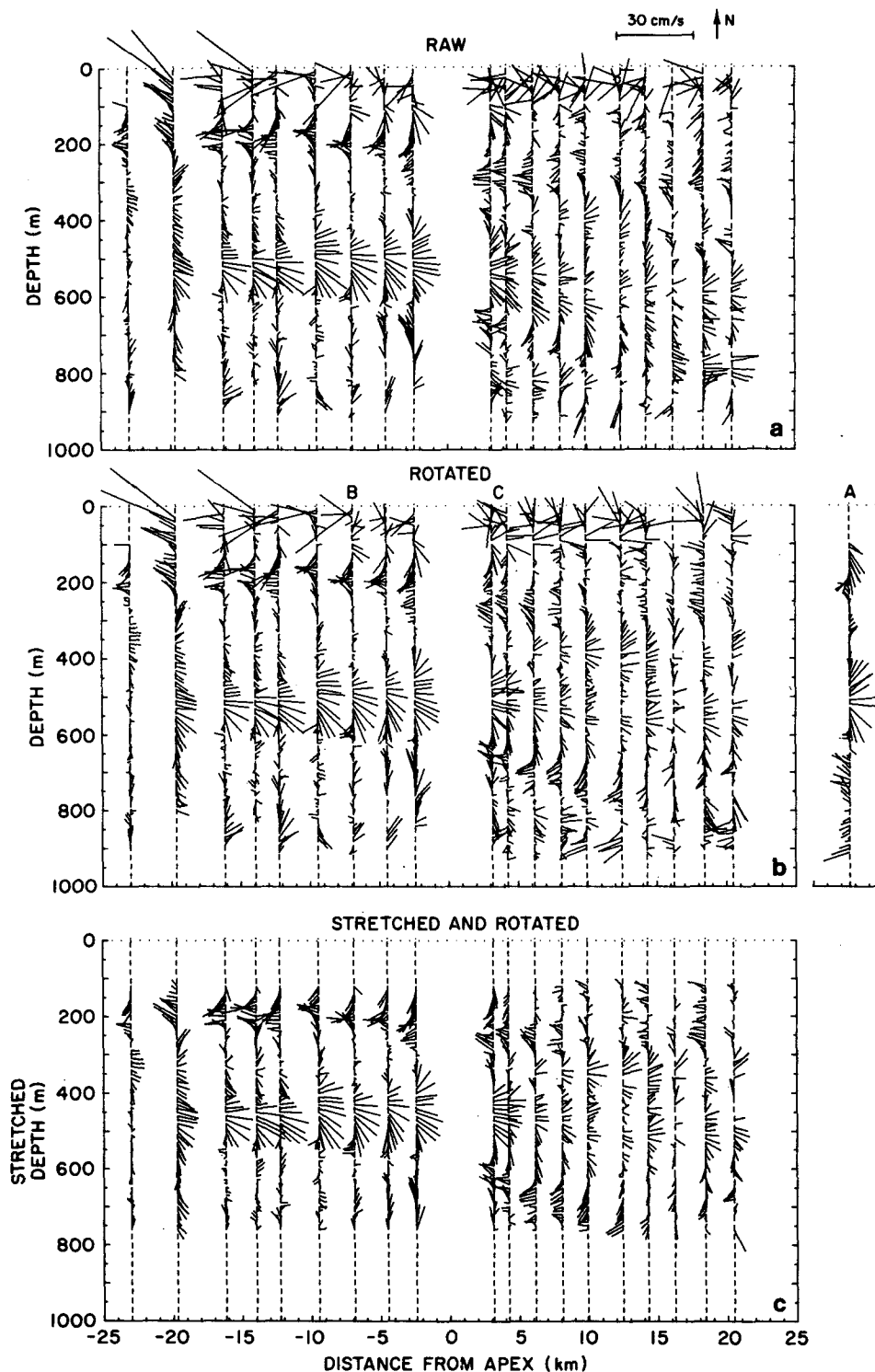


FIG. 2. XCP survey starting 1982 GMT 7 September. (a) Raw profiles. Velocity vectors are plotted every 5 m with magnetic north vertical. Horizontal position of vector indicates its position on bottom axis. (b) Profiles inertially rotated to common time. (c) Profiles WKB-stretched to 2 cph and rotated. Only data from 120 to 760 m are shown. Profiles A, B and C refer to Fig. 1.

fixed with respect to the water. This experiment occurred in a region of little vertical or horizontal shear so that an advection velocity constant in space and time has been used to transform the geographical profile positions (Fig. 1a) to the advected positions (Fig. 1b). Notice that profiles A and C (Fig. 2b) have the same geographical position, but A and B have the same advected position. The greater similarity of A and B confirms that the waves are indeed advected by the mean flow. All subsequent analysis is conducted using the advected positions.

3. Current meter data

A subsurface mooring containing eight vector-averaging current meters was deployed by the U.S. Naval Oceanographic Office at $30^{\circ}29.7'N$, $71^{\circ}45.6'W$ near the vertex of the L-shaped XCP tracks (Fig. 1a). Current measurements were made from 4 September to 6 October 1979 between 132 m and 372 m depth, which included the lower portion of the seasonal thermocline and most of the $18^{\circ}C$ water beneath it. Preliminary descriptions of these data have been given by Perkins (1980).

For the duration of the XCP drops, days 250–253, the mean current is very uniform in both depth and time and so provides a simple definition for the advected coordinate system used in the XCP analysis. The very low mean speeds during the second half of the data set can be seen in time series plots to result in stalling of the instrument rotors during an appreciable fraction of each inertial period. (A value of 2 cm s^{-1} , the nominal rotor stall speed, was assigned to the speeds during intervals when the instrument reported zero speed.) Two consequences stem from this. First, some systematic variation in mean speed can be noted between instruments, especially among the upper four instruments toward the end of the record. The effect arises from variation in stall speed between the rotors. Second, and more important for this analysis, is the distortion of the wave form caused by “bottom clipping” of the speeds. Using the analysis of Ruddick (1977), noise due to clipping will significantly bias spectral estimates after day 275. In the rest of the record, clipping will have a negligible effect—both because of the small fraction of time occupied by clipped data ($\sim 7\%$), and because the noise occurs primarily in the anticlockwise velocity component.

Spectra from the current meter data typically display (Fig. 3) the expected peak at the inertial frequency in the clockwise rotating component and at the semidiurnal frequency in both rotary components. It is not possible to distinguish between the diurnal and inertial frequencies; here as elsewhere in this paper, the term inertial includes both. As will be shown, the energy in this band has its origins near the surface which argues against its being tidally driven.

A demodulation technique (Perkins, 1972) has been

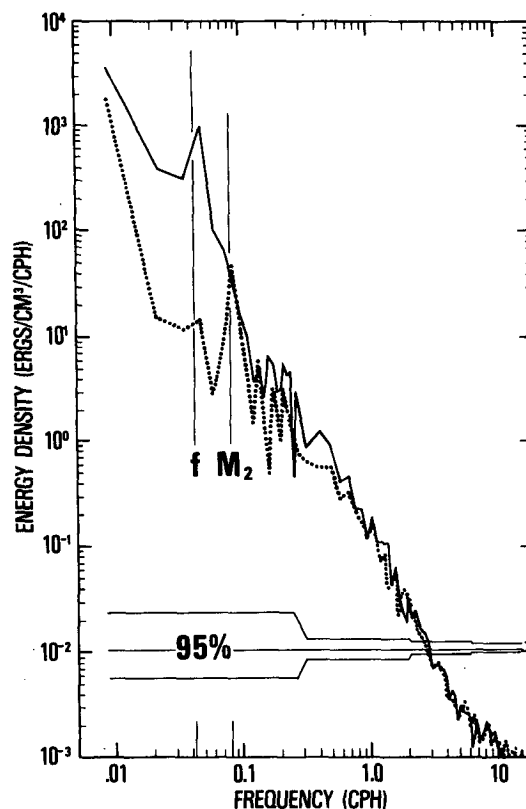


FIG. 3. Spectrum of circularly polarized clockwise (solid line) and anticlockwise (dotted line) current components from current meter at 222 m depth from days 248–275.

applied to the data to trace the time evolution of inertial motion; i.e., the components of current which have an inertial period and which are circularly polarized in the clockwise sense. Each current meter record was divided into 2-day segments with consecutive segments overlapping by 1 day. The mean and trend were removed from each segment, which was then Fourier transformed to extract the inertial component. Plotting the amplitude of this component for each segment gives the time evolution of the inertial motion seen in Fig. 4.

Two events dominate the demodulation amplitudes, one at the start of the data set near day 250 and the other between days 260 and 265. The latter reaches its peak value at progressively later times at greater depths, the corresponding downward propagation being some 20 m day^{-1} . During this second event, the variation in time of the phase of the inertial component indicates a wave frequency of about $1.04f$, and the variation of phase with depth suggests a vertical wavelength of 300 m. Combining these estimates in Eq. 2b yields a vertical group velocity of about 24 m day^{-1} . A more systematic analysis of the data in terms of vertically propagating waves will be given in Section 5.

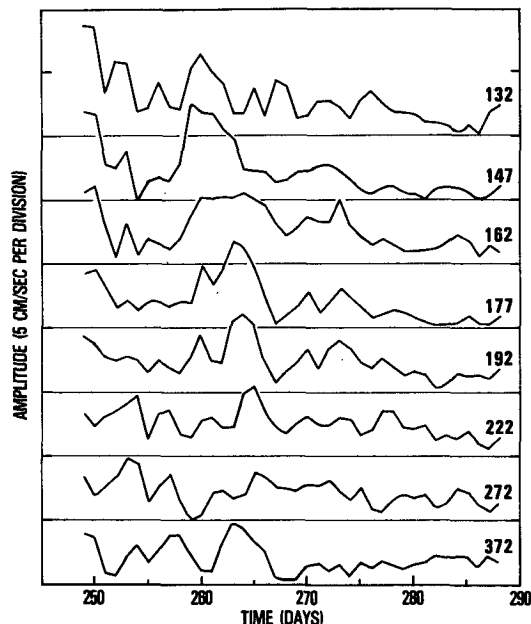


FIG. 4. Amplitude vs. time for the circularly polarized, inertial-period component of current for each of the eight current meter records. Horizontal lines give the zero for each trace with successive curves offset by 5 cm s^{-1} . Instrument depths in meters are given at the right.

4. Wavenumber–frequency spectra from profiler data

a. Analysis technique

An estimate of the internal wave wavenumber–frequency spectrum is made below using the space-time array of velocity profiles. The analysis assumes that the measured velocity fluctuations are due entirely to linear internal waves, and that these waves propagate in a time-independent ocean with no geostrophic shear and a Väisälä frequency that varies only with depth.

The first step in this procedure is to express each profile as the sum of orthogonal solutions of the internal wave equations. Ideally, the vertical internal-wave modes periodic on the domain of the profiles should be used as the expansion set. These functions are complete and thus completely describe the data (Hildebrand, 1976, p. 205). If the Väisälä frequency varies only slowly with depth, a close approximation to this expansion is obtained by applying a WKB stretching transform to each profile (Leaman and Sanford, 1975).

$$z_s = \int_0^z \frac{N(z)}{N_0} dz, \quad (3a)$$

$$\left. \begin{aligned} u_s(z_s) &= u(z)[N(z)/N_0]^{-1/2} \\ v_s(z_s) &= v(z)[N(z)/N_0]^{-1/2} \end{aligned} \right\} \quad (3b)$$

for Väisälä profile $N(z)$ and reference frequency N_0 . In the stretched variables u_s, v_s, z_s , the periodic internal wave solutions are nearly sinusoidal, so that a Fourier

transform in z_s yields approximately the correct modal amplitudes. The computed amplitudes will be called wavenumber amplitudes and labeled by β . This technique maps the unknown vertical mean of the unstretched velocity profile onto a nonconstant curve and thus will introduce noise into the lowest wavenumbers.

An average Väisälä profile $N(z)$ was computed from 12 CTD profiles (Perkins, 1980) taken during the XCP survey (Fig. 5). Over the depth range from 120 to 760 m the average Väisälä frequency is 2.0 cycles per hour (cph). A value of $N_0 = 2$ cph therefore results in stretched profiles (such as those in Fig. 2c) spanning the same depth range as the unstretched profiles. All other figures, however, are plotted with the more conventional value $N_0 = 3$ cph.

One check on the validity of WKB-scaling is the depth variation of kinetic energy. The unstretched horizontal kinetic energy varies as $N(z)$ (Fig. 5), in agreement with WKB scaling. The stretching transformation (3) will remove this variation and result in a data set nearly homogeneous in depth.

The wavenumber amplitudes are computed by taking the complex stretched velocity for profile k

$$U_k(z_s) = u_{s,k}(z_s) + iv_{s,k}(z_s), \quad (4)$$

multiplying it by a 50% Tukey window (Harris, 1978), Fourier transforming with respect to z_s and converting to $N_0 = 3$ cph to form complex Fourier amplitudes $\tilde{U}_k(\beta)$ for each vertical wavenumber β . Here $\tilde{U}_k(\beta)$ is

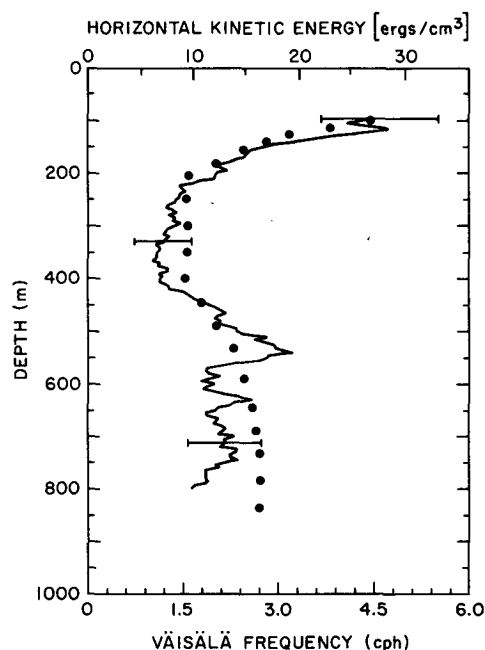


FIG. 5. Average energy for XCP profiles (top axis; line) and Väisälä frequency (bottom axis; dots). The 95% confidence limits are shown for energy.

taken to be the amplitude of wavenumber β for profile k at a reference Väisälä frequency of 3 cph.

The spectrum $|\hat{U}_i(\beta)|^2$ indicates the energy and vertical propagation direction of the waves at each scale if the spectrum is dominated by waves of near-inertial frequency (see Appendix C). The velocity component that rotates clockwise with increasing depth propagates downward; the component that rotates anticlockwise with increasing depth propagates upward. The spectrum for these data (Fig. 6) shows a dominance of clockwise energy at all but the smallest scales. This strong asymmetry is typical of western North Atlantic velocity profiles (Leaman 1976; Sanford 1975; Gregg and Sanford, 1980).

A complete spectral description of the internal wave field is obtained by specifying the horizontal wavenumber spectrum for each of the vertical wavenumbers. With sufficiently dense data, such a spectrum could be calculated by taking a two-dimensional spatial Fourier transform of the spectral amplitudes $\hat{U}_k(\beta)$. The present data are only dense enough to estimate the wavenumber-magnitude spectrum, a one-dimensional projection of the horizontal wavenumber spectrum. This, however, is sufficient to compute the frequency spectrum and the vertical, but not the horizontal, energy flux.

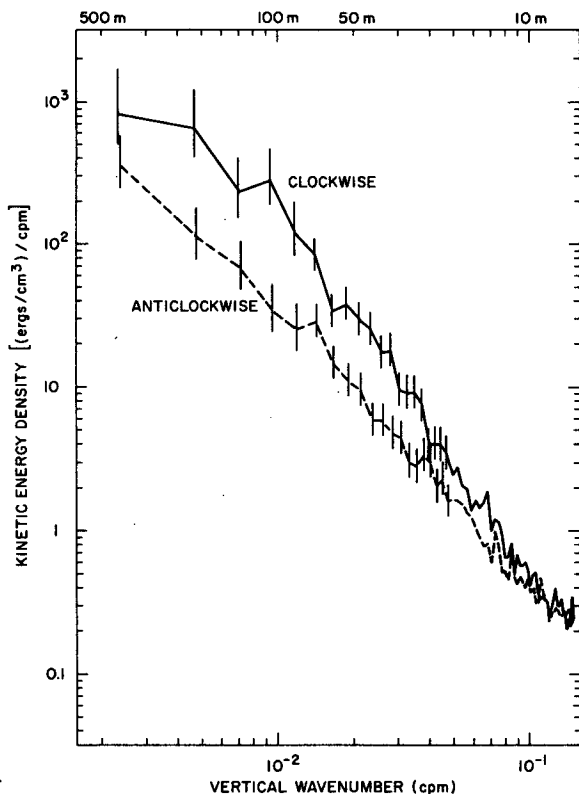


FIG. 6. Vertical wavenumber spectrum of WKB-stretched profiles ($N_0 = 3$ cph). The 95% confidence limits were computed as in Appendix D.

For a given vertical wavenumber β , with horizontal wavenumber-magnitude spectrum $E(\beta, \alpha)$, the cross-spectrum of complex velocity at spatial lag Δr is

$$C(\beta, \Delta r) = \langle \hat{U}(\beta, \vec{x}) \hat{U}^*(\beta, \vec{x} + \vec{r}) \rangle; \quad |\vec{r}| = \Delta r, \quad (5a)$$

$$= \int_0^\infty E(\beta, \alpha) J_0(\alpha \Delta r) d\alpha \quad (5b)$$

(Garrett and Munk, 1972), where J_0 is a Bessel function and \hat{U}^* is the complex conjugate of \hat{U} . Since only one profile was taken at a time, no purely spatial separations exist in the data; any two profiles are separated by both a space lag and a time lag. Despite this, $C(\beta, \Delta r)$ can be estimated from the data as described in Appendix A. Briefly, only profile pairs dominated by the spatial, as opposed to temporal, lag are used. The profiles are assumed to have frequency $\sigma = f$, and all are back-rotated to a common reference time. Because of the rapid speed of the survey relative to the phase speed of the waves, most profile pairs can be used. With $C(\beta, \Delta r)$ computed in this way, (5b) can be inverted by expanding $C(\beta, \Delta r)$ in a series of orthogonal Bessel functions,

$$C(\beta, \Delta r) = \sum_i E_i(\beta, \alpha_i) J_0(\alpha_i \Delta r). \quad (6)$$

Here $E_i(\beta, \alpha_i)$ is a discrete energy spectrum and completely describes the correlation function $C(\beta, \Delta r)$. Eq. 6 can be alternatively written in terms of discrete frequencies and vertical wavenumber by using (1),

$$C(\beta, r^*) = \sum_i E_i(\beta, \sigma_i) J_0 \left[\left(\frac{\sigma_i^2}{f^2} - 1 \right)^{1/2} r^* \right], \quad (7)$$

where

$$r^* = \frac{\beta f}{N} \Delta r$$

is the spatial separation, scaled by the vertical wavenumber. The inversion of (6) or (7) is implemented using the Bessel-function analog of the Blackman-Tukey Fourier transform (Blackman and Tukey, 1958) and may be called a Bessel transform (see Appendix A). The close analogy to a Fourier transform implies that most of the standard techniques of Fourier analysis can be used. The smallest resolvable, nonzero wavenumber is equal to $3.8/L$, where L is the maximum value of Δr . The largest wavenumber resolvable is roughly the Nyquist wavenumber $\pi/(\delta r)$, where δr is the sampling interval for $C(\beta, \Delta r)$.

Coherence functions and the associated horizontal wavenumber or frequency spectra have been computed for two vertical wavenumber bands, wavenumbers 1 and 2 (Fig. 7) and wavenumbers 3, 4 and 5 (Fig. 8), for both clockwise and anticlockwise wavenumbers. Several vertical wavenumber estimates were combined to increase the statistical reliability of the spectral estimates. Vertical wavenumbers larger than 5 (wave-

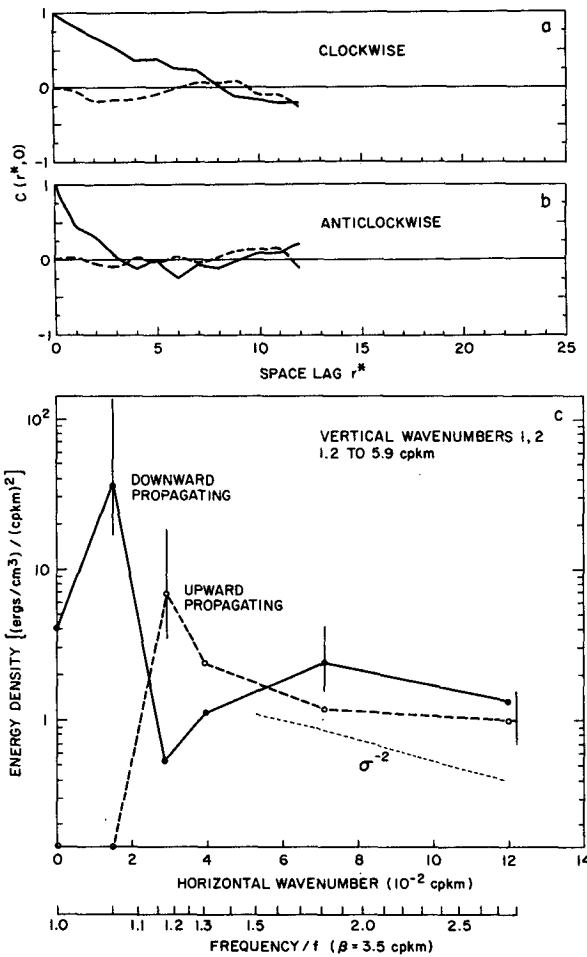


FIG. 7. (a) Real (solid) and imaginary (dashed) parts of estimated velocity coherence function for clockwise wavenumbers 1 and 2. (b) Same as (a) but for anticlockwise component. (c) Energy spectrum computed from real part of coherence function. This can be interpreted as either a horizontal wavenumber-magnitude spectrum (top axis) or an energy-preserving frequency spectrum (bottom axis). The 95% confidence limits are shown. The light dashed line shows a frequency $^{-2}$ spectrum in these coordinates.

length = 85 m at $N_0 = 3$ cph) have horizontal coherence scales smaller than the 2-km minimum separation of the profiles. For these waves $C(\beta, \Delta r)$ cannot be estimated.

One check on this procedure is obtained by noting that (7) requires $C(\beta, r^*)$ to be real. The real part of $C(\beta, r^*)$ (solid lines in Figs. 7a, b and 8a, b) is in fact much larger than the imaginary part of $C(\beta, r^*)$ (dashed lines) for both wavenumber bands.

The Bessel transform of $C(\beta, r^*)$, using (6), gives the internal wave energy as a function of either horizontal wavenumber or frequency for each vertical wavenumber. For σ near f , the energy in the clockwise and anticlockwise wavenumbers corresponds to downward and upward going energy. For $\sigma > f$, this is only approximately true. Given the clockwise and

anticlockwise frequency spectra for a given vertical wavenumber, it is possible, however, to construct the upward and downward going frequency spectra exactly, as described in Appendix C. These spectra are plotted in Figs. 7c and 8c. The confidence limits for the spectral estimates are computed by dividing the total degrees of freedom equally between the spectral estimates as described in Appendix D.

b. Results

The major result of the velocity profile analysis is the internal-wave frequency spectra for two vertical wavenumber bands (Figs. 7c, 8c). These have been computed from spatial correlation functions (Figs. 7a, b and 8a, b) of velocity assuming internal wave dynamics. Within each vertical wavenumber band, the energy has been divided into downward (solid line) and upward (dashed line) propagating components. Each spectrum can be interpreted either as a horizontal wavenumber (upper axis) or frequency (lower axis)

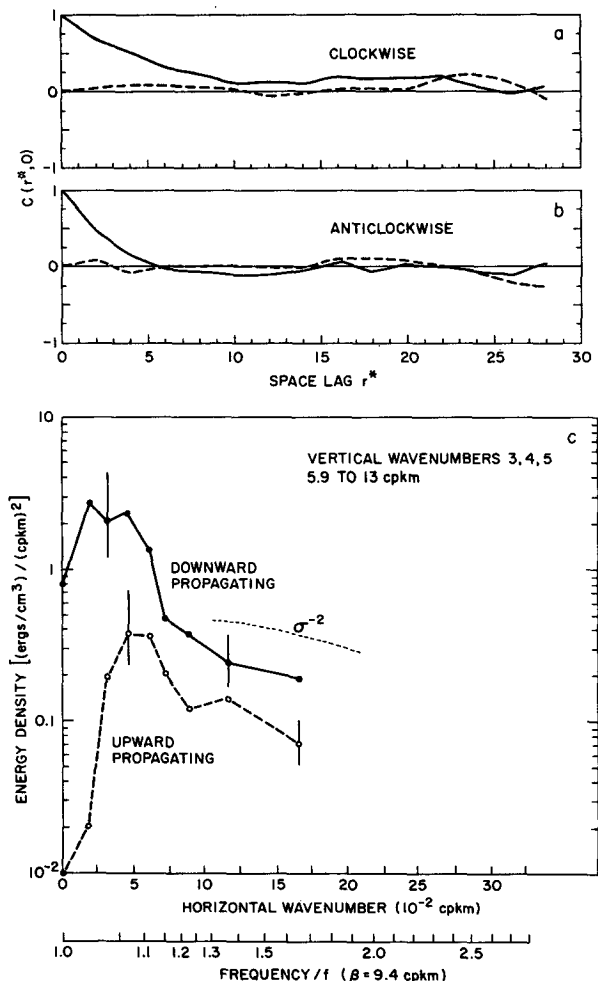


FIG. 8. As in Fig. 7 but for wavenumbers 3, 4 and 5.

spectrum. The different resolution of the spectra in the two vertical wavenumber bands reflects the different size of the sampling array relative to the horizontal scale of the waves and a different amount of band-averaging.

All of the computed frequency spectra are dominated by an inertial peak. Roughly 65% of the total kinetic energy is at frequencies less than $1.2f$. The downward propagating energy spectrum in both wavenumber bands has a peak centered at about $1.06f$ which contains about 70% of the kinetic energy. The upward propagating energy spectrum, in contrast, has an inertial peak with a significantly higher frequency, $1.16f$ for the first band and $1.08f$ for the second. The fraction of the total energy in this peak is less, only about 40%, and there is little energy at frequencies between the peak frequency and f . At frequencies higher than the inertial peak, the spectra are roughly consistent with a σ^{-2} spectrum shown by the light dashed lines in Figs. 7c and 8c. In the first wavenumber band, the higher frequencies are roughly symmetric so that all of the excess downward propagating energy is near the inertial frequency. The second wavenumber band has more downward energy at all frequencies up to its maximum frequency, $1.6f$.

The near-inertial internal wave field described by these measurements exhibits a profound vertical asymmetry. Not only is most of the energy propagating downward, as has been observed previously (Müller *et al.*, 1978; Leaman, 1976), but the downward going energy has a larger inertial peak and a typical frequency closer to the inertial frequency. Equivalently, the downward energy has a larger horizontal scale than the upward going energy, as can easily be seen from the correlation functions (Figs. 7a, b and 8a, b).

The vertical energy flux F has been computed for each wavenumber–frequency bin (Table 1) using

$$F = \left[\frac{2\sigma^2}{\sigma^2 + f^2} E(\alpha) \right] \cdot \left[\frac{\sigma^2 - f^2}{\sigma} \left\langle \frac{1}{\beta} \right\rangle \right], \quad (8)$$

where the first grouping is the total internal wave energy computed from the horizontal kinetic energy $E(\alpha)$ and the second grouping is the group velocity averaged over each vertical wavenumber band. Both $E(\alpha)$ and $\langle 1/\beta \rangle$ are largest in the first wavenumber band which thus dominates the flux estimate. Although most of the energy is near inertial, the group velocity increases as $\sigma - f$, so that the less energetic waves with $\sigma > 1.5f$ have as much influence on the total energy flux as the near-inertial waves. These higher frequency spectral estimates may, however, be contaminated with noise or spectral leakage. It seems safer, therefore, to compute only the near-inertial energy flux ($\sigma < 1.3f$), especially given the evidence from the current meter data of vertical symmetry for $\sigma > 1.3f$.

The measurements indicate a net near-inertial energy flux of 0.12 ± 0.12 ergs $\text{cm}^{-2} \text{s}^{-1}$ directed downward

TABLE 1. Near-inertial energy flux.

σ/f	Vertical group speed (cm s ⁻¹)	Energy (ergs cm ⁻³)		Vertical energy flux (10 ⁻² ergs cm ⁻² s ⁻¹)	
		up	down	up	down
<i>Wavenumbers 1, 2</i>					
1.05	0.09	0	2.27	0	21
1.16	0.28	0.46	0.04	<u>13</u>	<u>1</u>
				13 ± 5	22 ± 11
<i>Wavenumbers 3, 4, 5</i>					
1.009	0.005	0.002	0.273	0	0.15
1.031	0.019	0.022	0.211	0.04	0.39
1.064	0.039	0.042	0.241	0.16	0.94
1.107	0.067	0.042	0.145	0.28	0.97
1.160	0.103	0.025	0.053	0.26	0.54
1.222	0.121	0.014	0.042	<u>0.17</u>	<u>0.51</u>
				0.91 ± 0.3	3.5 ± 1.1
<i>Wavenumbers 1-5</i>					
		0.61	3.28	14 ± 5	26 ± 11
Net flux 0.12 ± 0.12					

(Table 1). This is the sum of 0.26 ± 0.11 ergs $\text{cm}^{-2} \text{s}^{-1}$ downward flux and 0.14 ± 0.05 ergs $\text{cm}^{-2} \text{s}^{-1}$ upward flux; the error limits here represent one standard deviation. Thus, although there is more than five times as much energy going downward as going upward, the upward going energy has almost three times the group velocity as the downward going energy and therefore only about half the flux. With the computed errors and Gaussian statistics, there is roughly a 16% chance that the net flux is upward. Even if the flux were zero, this would not imply that the wave field is symmetric; the upward and downward going energies clearly have different frequency spectra.

The energy flux estimate includes energy only from a limited range of vertical wavenumbers. Since both the energy and group velocity decrease with increasing vertical wavenumber, it seems unlikely that the larger vertical wavenumbers will contribute significantly to the vertical energy flux. Smaller wavenumbers, however, may be important. Sanford (personal communication, 1983), using 100 surface-to-bottom velocity profiles, finds a peak in the vertical wavenumber spectrum at roughly $1/300$ cpm, a scale comparable to the lowest wavenumber resolved here. However, if 75% of the total energy were resolved in this analysis, and the remaining 25% had a stretched vertical wavelength of 1.3 km (roughly mode 3) and the same frequency spectrum as shown in Fig. 7, the total energy flux would be twice that computed here. Internal waves with vertical wavelengths longer than those resolved in this analysis may therefore carry as much energy flux as the waves resolved here.

5. Frequency-wavenumber spectrum from current meter data

The vertical distribution of the eight current meters permits a description of the wave field in stretched vertical wavenumber β as well as in frequency. Thus, if the components of horizontal current are

$$(u, v) = \text{Re}\{(u_0, v_0)e^{i(kx+ly+\beta z-\sigma t)}\}, \quad (9)$$

then the total mean energy density at frequency σ and wavenumber β can be written (see Appendix B)

$$\langle E \rangle = \frac{1}{2} \frac{\sigma^2}{\sigma^2 + f^2} \frac{N^2 - f^2}{N^2 - \sigma^2} (u_0 u_0^* + v_0 v_0^*). \quad (10)$$

With z directed upward and σ taken as positive, the vertical component of energy flux is upward for negative β and downward for positive β . This method provides a direct evaluation of the frequency-wavenumber spectrum under the assumption that the observations are propagating waves, but does not provide for a test of that assumption—as would be possible if measurements of vertical displacement or velocity were available (Müller and Siedler, 1976; Müller *et al.*, 1978). Decomposition of the observed currents into frequency and wavenumber components was carried out first by Fourier-analyzing each record in time from day 248 to 275 using 4-day-long, half-overlapped pieces to which a Hanning window had been applied (Welch, 1967) and, second, by least-squares fitting of the Fourier coefficients by sinusoidal functions of stretched depth and prescribed vertical wavenumbers.

Two principal advantages of the least-squares procedure are that it can accommodate without interpolation the unequal spacing of the instruments, and that it provides a linear statement about wavenumber resolution. A least-squares coefficient u_n corresponding to vertical wavenumber β_n can be represented in terms of the true spectrum $u(\beta)$ by

$$u_n = \int_{-\infty}^{\infty} u(\beta) h_n(\beta) d\beta,$$

where the function h_n is a spectral window, or admittance, which depends on the vertical grid and on the total collection of wavenumbers used in the analysis. Unlike the case for regularly spaced data, there will be a different response window h_n for each wavenumber β_n , each having the general properties

$$h_n(\beta_m) = \begin{cases} 1 & \text{if } n = m \\ 0 & \text{if } n \neq m. \end{cases}$$

For the analysis of the current meter data, the wavenumbers were chosen as

$$\beta_n = \frac{2\pi n}{\Delta Z}, \quad n = -2, -1, 0, 1, 2,$$

where ΔZ is 432 stretched decibars, the distance between the deepest and shallowest instruments. Mag-

nitudes $H_n(\beta)$ of the corresponding complex response functions $h_n(\beta)$ are given in Fig. 9. Within the analysis band of ± 4.6 cycles per stretched kilometer, the response heavily emphasizes a band around the appropriate wavenumber, as is required. Outside the analysis band, the side lobes are comparable to the main lobe, indicating a potential problem with the spectral leakage. Since the typical vertical wavenumber spectra decay as $\beta^{-2.5}$ (Fig. 6), leakage into the bands with $n = 0$ and $n = \pm 1$ from higher wavenumbers will be small. Leakage into the $n = \pm 2$ bands from lower wavenumbers may be significant.

For the inertial-period component of motion, application of this technique leads to Fig. 10. The two energetic events already noted in Fig. 4, one at the start of the record and the other during days 260–265, appear here as having downward energy flux with vertical wavenumbers near 2.3 cycles per stretched kilometer. For the latter event, this result, which depends on the wave polarization, is independent of the apparent downward propagation of a packet that was noted earlier. The evidence in Fig. 10 for upward propagation near day 260 must be considered equivocal because of the possibility of spectral leakage. Each estimate in this periodogram presentation has 4 degrees of freedom.

The application of this technique to several frequency bands leads to the wavenumber-frequency spectrum in Fig. 11. Two prominent peaks are seen at the inertial and M_2 tidal frequencies. As in Fig. 10, the inertial frequency is primarily downward propagating. The M_2 tidal velocities show no energy except at zero wavenumber. Detailed analysis of the M_2 tidal records taken during the MODE (Zetler *et al.*, 1975) and IWEX (Müller *et al.*, 1978) experiments shows

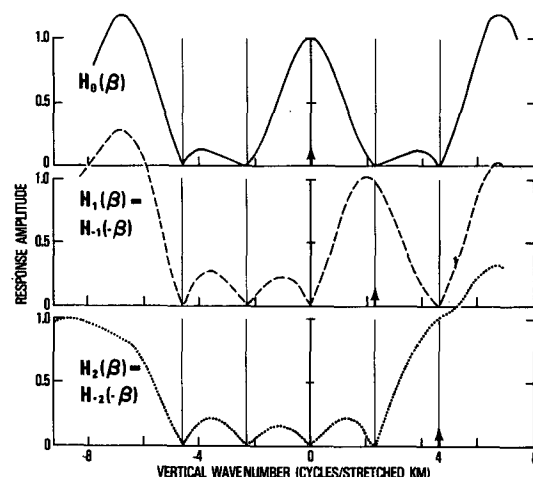


FIG. 9. Response functions $H_n(\beta)$ for the five vertical wavenumbers used in the analysis. Because of the indicated symmetry, it suffices to show three of the five traces. Wavenumbers used in the analysis are indicated by vertical dashed lines, and the particular wavenumber to which each curve applies is indicated by an arrow.

TABLE 2. Comparison of XCP and current meter analysis.
CL denotes confidence limits.

	XCP*	Current meter**
Kinetic energy		
Total	6.6	10.3
95% CL	(5.6–7.7)	(8.2–12.6)
Upgoing	1.5	3.7
95% CL	(1.3–1.8)	(2.9–4.6)
% of total	23%	36%
95% CL	(19–27)	(29–43)
Downgoing	5.1	6.6
95% CL	(4.1–6.1)	(4.8–8.7)
% of total	77%	64%
95% CL	(72–82)	(55–73)
Inertial energy@		
Total	86%†	66%
95% CL	(82–90)	(57–75)
Upgoing	72%†	54%
95% CL	(64–80)	(43–65)
Downgoing	90%†	73%
95% CL	(86–94)	(63–83)
Peak frequency/f		
Upgoing	1.15†	1.2
CL	(1.10–1.23)	(0.80–1.6)#
Downgoing	1.05†	1.0
CL	(1.025–1.10)	(0.81–1.21)#

* Vertical mean removed.

** Energy in vertical wavenumbers outside of 2 cpkm.

@ Energy with frequencies between f and $1.5f$ for XCP, and between $0.75f$ and $1.5f$ for current meters.

† Lowest two wavenumbers only; higher wavenumbers do not resolve to a high enough frequency.

Computed from intersection of spectrum with lower 95% CL from peak.

different in terms of frequency and vertical-wavenumber resolution that a quantitative comparison is difficult. The inertial band will be defined as $0.75f$ to $1.5f$. This is sufficiently wide to encompass the inertial peak computed using the current meter data. Because of the limited record length, that peak will necessarily be at least $0.38f$ wide. This band is also sufficiently narrow to fit within the limited frequency range of the XCP analysis for the first wavenumber bin (Fig. 7). With the inertial band defined in this way, both analyses place much more than half of the total energy in the inertial peak. Both show the downward going energy to be significantly more inertial than the upward going energy. The XCP analysis places more energy in the inertial peak than does the current meter analysis. This may be due either to a bias of the XCP analysis, as is suggested by simulations, or to Doppler spreading of the inertial peak as measured by the current meters. Given typical horizontal wavenumbers of 0.04 cycles per kilometer (cpkm) and typical horizontal advection velocities of 10 cm s^{-1} , the frequency of a near-inertial wave will be Doppler-shifted by $0.3f$.

d. Inertial peak frequency

Both analyses show a near-inertial frequency peak in the frequency spectrum of both upgoing and downgoing energy. The central frequency of this peak is higher for the upgoing energy ($\sim 1.1f$ – $1.2f$) than for the downgoing energy ($\sim 1.05f$). This feature is clear in the XCP analysis and is marginally resolved in the current meter analysis. Given the current meter results alone, this feature would not be statistically significant, as the confidence limits in Table 2 demonstrate. The large, downward propagating, inertial feature on day 260 of the current meter record has a frequency of about $1.04f$, which agrees well with the inertial-peak frequency computed in the XCP analysis.

e. Conclusion

The two measurement techniques compared here emphasize different parts of the internal wave spectrum. Current-meter time series easily provide an accurate frequency spectrum integrated over wavenumber. Several current meters spaced vertically will allow a vertical wavenumber–frequency spectrum to be computed. Unless the time series is many months long, however, this technique will not provide sufficient frequency resolution to resolve the details of the inertial peak. Vertical profilers, such as the XCP, easily provide a signed vertical wavenumber spectrum integrated over frequency. If these are deployed in a horizontal array, a frequency spectrum of internal waves near the inertial frequency can be computed comparable in resolution to that obtained from year-long current meter records. Such resolution in frequency, plus signed vertical wavenumber resolution, is required to compute the vertical energy flux. The price for this high resolution near the inertial frequency is a limited ability to resolve higher-frequency waves.

These two techniques have been compared here. In the limited regime, where their results overlap, qualitatively similar results are found. The quantitative differences appear to result from intrinsic biases in both methods and from the intermittency of the measured internal wave signal.

7. Wind forcing

A dominant feature of these data is the difference between the upward and downward going internal waves. The net flux appears to be downward, which suggests a surface source. The downward going waves have a larger horizontal scale, consistent with the large scale of atmospheric forcing. Are wind-generated inertial oscillations in the mixed layer the source for these waves, as suggested by Pollard (1969, 1980)? The energy flux input into mixed-layer inertial oscillations was estimated by driving the mixed layer model of Pollard and Millard (1970) with the surface winds measured by the NDBO meteorological buoy at

32.3°N, 75.3°W, roughly 360 km northwest of the site of this experiment (Hamilton, 1980). The drag coefficient of Garratt (1977), a damping time of 1 day, and a mixed layer depth of 35 m were used. The computed energy flux is insensitive to the damping time and inversely proportional to the mixed layer depth. The average computed energy flux from 1 June to 10 September 1979 was $0.18 \text{ ergs cm}^{-2} \text{ s}^{-1}$, which is of the same order as the estimated net downward energy flux in the wave field. A large fraction of the energy put into the mixed-layer inertial currents by the wind appears to propagate out of the mixed layer as internal waves.

This result presents several puzzles. For a linear f -plane model such as Pollard's (1969), wind-forced internal waves are created with a horizontal scale that matches that of the wind. Assuming that the inertial peak for the downward going waves is wind forced, these models would imply a dominant horizontal wavelength for the inertial frequency component of the wind stress of about 70 km for the first wavenumber band and 26 km for the second. The dominant scales of variation in the atmosphere are much larger than this (Willebrand, 1978). Possible explanations for this discrepancy include a strong role for mesoscale atmospheric disturbances, the impression of oceanic mesoscale motions on the internal-wave generation mechanism (Weller, 1982) or the influence of the β -effect (Fu, 1981).

The downward flux divided by the downward going energy yields an average group velocity of approximately 70 m day^{-1} . Energy put in at the surface would thus take about a week to traverse the depth range measured here. For purely linear dynamics, the vertical homogeneity of the data thus requires an input of internal wave energy at the surface uniform from week to week. Given the observed intermittency of storms, such a uniform forcing regime seems unlikely. Some other factor, perhaps the influence of the mesoscale eddies, may play a role in maintaining the observed vertical uniformity of the internal waves.

8. Conclusions

- Two independent estimates of the wavenumber-frequency spectrum for near-inertial internal waves, one using a moored current-meter string and a second using a space-time pattern of velocity profiles, are qualitatively consistent. This verifies the internal-wave dispersion relationship for near-inertial waves and demonstrates the power of a space-time velocity-profile survey to resolve the details of the near-inertial internal-wave spectrum and to estimate its energy flux.

- The internal wave field during these measurements was dominated by near-inertial frequency waves with a net downward energy flux of $0.12 \pm 0.12 \text{ ergs cm}^{-2} \text{ s}^{-1}$ in the vertical wavenumber band, 1.2 to 13 cpkm

(stretched to 3 cph), which is the sum of $0.26 \pm 0.1 \text{ ergs cm}^{-2} \text{ s}^{-1}$ downward flux and $0.14 \pm 0.05 \text{ ergs cm}^{-2} \text{ s}^{-1}$ upward flux. Roughly five times as much energy is propagating downward as upward, but this is partially compensated by the faster group velocity of the upward going energy (200 m day^{-1}) as compared to the downward going energy (70 m day^{-1}). These differences reflect different peak frequencies for the upward and downward going waves, $\sim 1.1f$ and $\sim 1.06f$, respectively. These estimates may differ from the total energy flux by a factor of 2 because of flux in unresolved, long vertical-wavelength waves.

- The near-inertial energy flux roughly balances the estimated input of energy by the wind fluctuations into inertial surface currents, which suggests that the wind is a major source of near-inertial internal waves.

- The internal wave field in these observations is symmetric at frequencies above 1.5 times the inertial frequency.

9. Discussion

Fu (1981), using long-term current meter records from the western North Atlantic, suggests that the near-inertial wave field is the superposition of a vertically symmetric, broadband background component, plus a locally generated, downward propagating, near-inertial component. The data presented here generally support this scenario. The measured wave field is asymmetric only very near the inertial frequency; the excess downward propagating energy is of a larger scale than the upward propagating energy, consistent with large-scale surface forcing. Our inertial peak widths, $0.1f$, are roughly consistent with Fu's, but our peak heights, 25 db above the continuum, are somewhat greater. Fu's data suggest an inertial peak within 2% of f , at 500 m. This is inconsistent with the measurements presented here and may represent the effect of spatial and temporal inhomogeneities in the wave field (Fu's measurements being year-long averages) or vertical gradients in the inertial-wave field properties between these measurements averaged over 120 to 760 m and Fu's measurements at 600 and 1000 m.

The data presented here are consistent with the theoretical predictions of McComas and Müller (1981). In these calculations, the internal wave field rapidly equilibrates to a vertically symmetric spectrum at all frequencies higher than inertial. Only near the inertial frequency are asymmetries due to energy sources and sinks preserved.

The profiler analysis presented here has assumed linear internal-wave dynamics. One measure of the accuracy of this assumption is the velocity U_c , needed to Doppler-shift a wave to the inertial frequency,

$$U_c = \sqrt{2} \frac{(\sigma - f)}{\alpha} = \sqrt{2} \frac{N}{\beta} \left(\frac{\sigma - f}{\sigma + f} \right)^{1/2},$$

as compared to the typical internal wave or mean velocity difference Δu in the ocean. If $U_c \gg \Delta u$, the wave can be considered linear; if $U_c \ll \Delta u$, it cannot. For any given vertical wavenumber, the most nonlinear waves by this criterion are those closest to the inertial frequency. Thus U_c should be evaluated at the inertial peak; U_c is 5.7 cm s^{-1} for the first wavenumber (Fig. 7) band and 2.1 cm s^{-1} for the second (Fig. 8). The rms velocity from the XCP profiles is 3.3 cm s^{-1} . Using this for Δu , $U_c/\Delta u = 1.7$ for the first band and 0.63 for the second. The general agreement of the profiler and current meter results suggests that these waves are sufficiently linear for their scales to obey the dispersion relation (1), which is all that the analysis requires. The analysis will probably fail at vertical wavelengths much smaller than 100 m.

It can be speculated that several details of the frequency spectra in Figs. 7 and 8 are related to this wave nonlinearity. In both bands, the upward going energy exhibits an inertial peak at a higher frequency than the downgoing energy and has a "dead band" with little energy very near f . Waves in this dead band would be the most nonlinear by the above criterion and might, therefore, be the most susceptible to breaking, scattering or other nonlinear processes that transfer their energy to other scales. Such an effect would be most apparent in the upward going waves, which have been subject to these effects longer than the presumably surface-generated, downward going waves. The same effect might account for the broadband excess of downward propagating energy in the second wavenumber band as opposed to the first. The inertial peak in the second band is more nonlinear and, assuming it is surface generated, has propagated in the ocean roughly three times longer than the inertial peak in the first band. The resulting nonlinearities may have acted to spread the originally sharp inertial peak over the range of frequencies observed.

These measurements span a limited space and time. The good comparison between the spatial measurements spanning a region 20 km by 60 km and the temporal measurements spanning 50 days at one location suggests that these results are typical of the late-summer Sargasso Sea. The observed vertical asymmetry seems typical of other less detailed measurements in this area (Leaman, 1976; Müller *et al.*, 1978). Other profiler data not presented here (D'Asaro, 1983) suggest that it is not typical of all places and times.

Acknowledgments. The data used here were taken under Naval Ocean Research and Development Activity Contract N00014-79-C-071 to the Applied Physics Laboratory, University of Washington. Analysis was supported by Office of Naval Research Contract N00014-80-C-0252 and the Ocean Measurements Program, Office of Program Management, NORDA Code 540. The senior author would like to thank T. Sanford for his continued support and encouragement.

APPENDIX A

Frequency Spectra from a Space-Time Velocity Profile Array

1. Spatial coherence function

Given complex wavenumber amplitudes of an internal wave field $\hat{U}_i(\beta)$, taken at position r_i and time t_i , we wish to estimate the spatial correlation function where $t_i = t_j$ only for $i = j$. We define an inertially rotated correlation function,

$$\hat{\gamma}(r^*, t^*) = \frac{\langle \hat{U}_i \hat{U}_j^* e^{-it^*} \rangle}{\langle |\hat{U}_i|^2 \rangle}, \quad (\text{A1})$$

where $t^* = f(t_j - t_i)$, $r^* = (\beta f/N)|\vec{r}_j - \vec{r}_i|$, U^* is the complex conjugate of U , and angle brackets denote an average over i, j . For a wave field with kinetic energy spectrum $E(\omega)$, the expectation value of $\hat{\gamma}$ for a perfect sampling grid is

$$\gamma(r^*, t^*) = \int_1^{N/f} E(\omega) J_0[(\omega^2 - 1)^{1/2} r^*] e^{-i(\omega-1)t^*} d\omega, \quad (\text{A2})$$

where $\omega = \sigma/f$; $\hat{\gamma}$ may differ from γ because of statistical variation or an imperfect sampling grid. We here describe an empirical scheme to compute $\hat{\gamma}(r^*, 0)$.

We anticipate the frequency spectrum will be the sum of an inertial peak with $\omega - 1 = \epsilon \ll 1$ and some broadband spectrum. For the inertial peak, $\gamma(r^*, t^*) = \gamma(r^*, 0) + O(\epsilon)$ as long as $\epsilon t^* \ll 1$. Modeling the continuum by $E(\omega) = 1/\omega^2$, the resulting values $\gamma_R(r^*, t^*)$, the real part of $\gamma(r^*, t^*)$, are shown in Fig. A1.

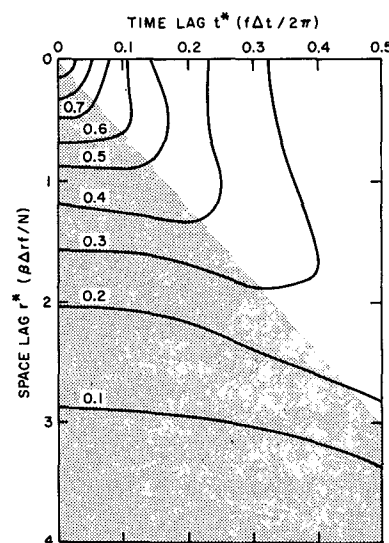


FIG. A1. Real part of coherence function as a function of space and time lag, for a frequency⁻² spectrum, inertially-rotated and assuming internal wave dynamics. Shaded area shows region dominated by spatial lag.

Within the shaded region, $\gamma_R(r^*, t^*) = \gamma_R(r^*, 0)$ with an error less than 0.1. The shaded region corresponds to $\Delta r/\Delta t > N/\beta$. For $r^* > 5$, $\gamma_R(r^*, t^*) < 0.1$. We compute $\hat{\gamma}(r^*, 0)$ using only those profile pairs for which $\gamma(r^*, t^*) \approx \gamma(r^*, 0)$. The criteria used are

$$\frac{\Delta r}{\Delta t} > \frac{N}{\beta} \quad \text{or} \quad r^* > 5. \quad (\text{A3})$$

Profile pairs with large temporal separations have an uncertainty in spatial separation because of the advected coordinate system. We therefore also require

$$\Delta t < 30 \text{ hours}, \quad (\text{A4})$$

which forbids pairs between the 10 September and 6–7 September surveys.

For this data set we have found conditions (A3, A4) to work well. Out of 4530 total cross-spectral pairs, 3781 (83%) were used. This reflects the rapid survey speed of the ship relative to N/β . The accuracy of the computed correlation functions is assessed below.

2. Bessel transforms

Given the spatial correlation function $C(\beta, \Delta r) = \hat{\gamma}(r^*, 0)$ at wavenumber β , we wish to expand it in an orthogonal sum of Bessel functions $J_0(\alpha_i \Delta r)$ as in (6). There are several possible orthogonal sets (Hildebrand, 1976, Eq. 5.13). The most convenient for our purpose satisfies the condition $J_0(\alpha_i L) = -J_1(\alpha_i L) = 0$, where L is the maximum lag of the correlation function. This set of α_i is complete for all correlation functions with $\partial C/\partial \Delta r = 0$ at $\Delta r = 0$ and $\Delta r = L$. It is preferred over other expansions because the constant function is a member of the set.

The expansion coefficients E_i are computed, using

$$E_i = \frac{2}{L^2 J_0^2(\alpha_i L)} \int_0^L W(r) C(\beta, r) J_0(\alpha_i r) r dr, \quad (\text{A5})$$

where $W(r)$ is a window used to taper $C(\beta, r)$ to zero at $r = L$. This procedure is analogous to the Blackman-Tukey Fourier transform (Blackman and Tukey, 1958). Unlike the more usual FFT windows, the side lobes from the window here can result in negative values of E_i . We have used a judicious combination of windows and band-averaging to preserve both the narrow inertial peaks and to remove their negative side lobes. As with Fourier transforms, the minimum resolvable wavelength is about twice the sampling interval. In constructing $C(\beta, \Delta r)$, there is a trade-off between the resolution of Δr , and therefore the maximum wavenumber, and statistical stability.

The values of E_i were found to be sensitive to the details of the integration (A5). $C(\beta, \Delta r)$ is largest near $r = 0$ where the integral norm r has the least weight. It was found that some integration schemes would completely ignore the value of $C(\beta, \Delta r)$ at $r = 0$, resulting in obviously false values of E_i . We evaluated

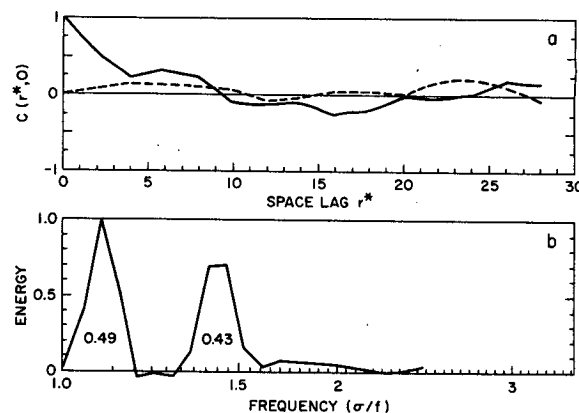


FIG. A2. Example of analysis procedure. An internal wave spectrum with energy 0.5 at $1.03f$ and $1.4f$ generates a coherence function (a), using the same profile positions, selection criteria, and notation as in Fig. 7. The resulting frequency spectrum (b) resolves both peaks with approximately the correct energy. The energy contained in each peak is displayed.

(A5) using a cubic spline interpolation of the symmetric extension of $C(\beta, \Delta r)$ on $[-L, L]$ to a grid 10 times finer than the digitization of Δr and then integrated trapezoidally on this fine grid.

The accuracy of this entire procedure is illustrated in Fig. A2. Each value of γ_{ij} for the second wavenumber band (Fig. 8) has been replaced by that corresponding to an energy spectrum with equal energy in peaks at $\sigma = 1.03f$ and $1.4f$. This preserves any biases associated with the array geometry and removes the statistical variability. The resulting frequency spectrum clearly resolves both peaks and correctly assigns about half of the energy to each. Notice, however, some loss of energy from the higher frequency peak. Side lobe energy is apparent, with an energy density of about 10% of the peak. The expansion (6) yields $C(0, 0) = 0.98$; about 2% of the energy is lost. This is a characteristic error; the expansions for Figs. 7c and 8c yield $C(0, 0) = 0.95$ and 0.87 , respectively.

APPENDIX B

Vertical Energy Propagation for Current-Meter Analysis

The Boussinesq internal wave equations with reference density $\rho_0 = 1$ can be written as

$$u_t - fv = -P_x, \quad (\text{B1})$$

$$u_t + fu = -P_y, \quad (\text{B2})$$

$$w_t + N^2 \xi = P_z, \quad (\text{B3})$$

$$\xi_t - w = 0, \quad (\text{B4})$$

$$u_x + v_y + w_z = 0, \quad (\text{B5})$$

where z is positive upwards and ξ represents vertical displacement from equilibrium. The energy density corresponding to this system is (Fofonoff, 1969)

$$E = \frac{1}{2} (u^2 + v^2 + w^2 + N^2 \xi^2). \quad (\text{B6})$$

Taking f and N as constant, solutions to (B1)–(B5) can be found as plane waves

$$(u, v, w, \xi, P) = \text{Re}\{u_0, v_0, w_0, \xi_0, P_0\} e^{i(kx + ly + \beta z - \sigma t)}. \quad (\text{B7})$$

The mean energy density, averaged over a wave cycle, can then be expressed as

$$\langle E \rangle = \frac{1}{4} (u_0 u_0^\dagger + v_0 v_0^\dagger + w_0 w_0^\dagger + N_0^2 \xi_0 \xi_0^\dagger), \quad (\text{B8})$$

where the dagger denotes complex conjugation.

The dispersion relation can be found by substituting (B7) into (B1)–(B5)

$$(k^2 + l^2)(N^2 - \sigma^2) = \beta^2(\sigma^2 - f^2). \quad (\text{B9})$$

The vertical group velocity of each plane wave is

$$C_{g3} = \frac{\partial \sigma}{\partial \beta} = \frac{1}{\sigma \beta} \frac{(N^2 - \sigma^2)(\sigma^2 - f^2)}{N^2 - f^2}. \quad (\text{B10})$$

It suffices to consider σ as positive. Hence, for frequencies in the internal wave band $N > \sigma > f$, the energy flux is upward if β is negative and downward if β is positive.

To evaluate the mean energy density $\langle E \rangle$ from measurements of horizontal current velocity, ξ_0 can be eliminated from (B8) by (B4)

$$\xi_0 \xi_0^\dagger = w_0 w_0^\dagger / \sigma^2, \quad (\text{B11})$$

and w_0 by (LeBlond and Mysak, 1978, Eq. 8.74)

$$w_0 w_0^\dagger = \frac{\sigma^2}{N^2 - \sigma^2} \frac{\sigma^2 - f^2}{\sigma^2 + f^2} (u_0 u_0^\dagger + v_0 v_0^\dagger). \quad (\text{B12})$$

Using (B11) and (B12), Eq. (B8) becomes

$$\langle E \rangle = \frac{1}{2} \frac{\sigma^2}{\sigma^2 + f^2} \frac{N^2 - f^2}{N^2 - \sigma^2} (u_0 u_0^\dagger + v_0 v_0^\dagger). \quad (\text{B13})$$

The energy flux may then be represented as the product of the mean energy density and the group velocity (LeBlond and Mysak, 1978, Eq. 8.77),

$$F_3 = C_{g3} \langle E \rangle = \frac{1}{2} \frac{\sigma}{\beta} \frac{\sigma^2 - f^2}{\sigma^2 + f^2} (u_0 u_0^\dagger + v_0 v_0^\dagger). \quad (\text{B14})$$

In practice, the energy density was determined by (B13) based on the Fourier transform of u and v with respect to depth and time, with the direction of flux given implicitly by the sign of the vertical wavenumber, as noted above.

APPENDIX C

Vertical Energy Propagation for Profiler Analysis

For the profiler (XCP) analysis it is preferable to compute spectra of the complex velocity (4), rather

than the u and v velocity components. In this case, the Fourier amplitudes $\tilde{U}_k(\beta)$ for positive (clockwise) and negative (anticlockwise) β correspond approximately, but not exactly, to the downward and upward propagating parts of the wave field. The transformations necessary to separate the downward and upward propagating waves exactly are described here.

Let the wave field be described by the superposition of waves given by the real part of

$$P = (P_+ e^{+i\beta z} + P_- e^{-i\beta z}) e^{i[kx + ly - \sigma(k, l, \beta)t]}. \quad (\text{C1})$$

Using (B4), in the hydrostatic limit $w \ll N$, the vertical energy flux can be written

$$\frac{1}{2} \overline{Pw} = \frac{\sigma \beta}{2N^2} (-|P_+|^2 + |P_-|^2), \quad (\text{C2})$$

where the overbar denotes an average over a vertical wavelength. The P_+ wave has a downward energy flux; the P_- wave has an upward flux. The energy corresponding to each of these waves is

$$E_\pm = \frac{1}{2} \frac{\beta^2}{N^2} \frac{\sigma^2}{\sigma^2 - f^2} |P_\pm|^2 = \frac{2\sigma^2}{\sigma^2 + f^2} (|\tilde{u}|^2 + |\tilde{v}|^2)_\pm, \quad (\text{C3})$$

and the total energy $E = E_+ + E_-$.

In the profiler analysis, we expand the complex velocity vector in terms of vertical wavenumber

$$u + iv = \tilde{U}_+ e^{i\beta z} + \tilde{U}_- e^{-i\beta z}. \quad (\text{C4})$$

\tilde{U}_+ and \tilde{U}_- do not correspond exactly to E_+ and E_- as denoted by the tilde. If we define

$$\tilde{E}_\pm = \frac{2\sigma^2}{\sigma^2 + f^2} |\tilde{U}_\pm|^2, \quad (\text{C5})$$

and find \tilde{E}_\pm in terms of P_\pm , then the true upward and downward propagating energies are found to be

$$E_\pm = \frac{(\sigma + f)^2}{4\sigma f} \tilde{E}_\pm - \frac{(\sigma - f)^2}{4\sigma f} \tilde{E}_\mp, \quad (\text{C6})$$

where P_+ and P_- are assumed uncorrelated, and (C3) has been used.

APPENDIX D

Confidence Limits

The data analyzed here are dominated by large space and time scales relative to the sampling intervals. Adjacent samples are therefore correlated, and the number of degrees of freedom of the data is much less than the number of measurements. Equivalently, the energy spectra are red so that the total energy is dominated by a small number of spectral estimates and, thus, by a small fraction of the total data. The techniques used to compute degrees of freedom and confidence limits for these data are described below.

Given a set of N_a uncorrelated spectral estimates E_i , each with degrees of freedom M_i , the number of degrees of freedom M for the total energy $E = \sum E_i$ is computed by assuming both E and E_i to be χ^2 distributed so that the variance of E is given by

$$\text{var}[E] = 2\bar{E}^2/M = \sum \text{var}[E_i] = \sum \frac{2E_i^2}{N_i}. \quad (\text{D1})$$

In this case,

$$M = \frac{(\sum \bar{E}_i)^2}{\sum \bar{E}_i^2/N_i}. \quad (\text{D2})$$

Confidence limits are now computed for \bar{E} using the χ_M^2 distribution.

For the profiler analysis, it is easier to work with the spatial correlation function rather than the horizontal wavenumber spectrum. Given N profiles with total energy E and correlation coefficient ρ_{ij} between profiles i and j , the number of degrees of freedom M for the energy estimate is

$$M = \frac{2N^2}{\sum_{ij} \rho_{ij}^2} \quad (\text{D3})$$

(Kang and Magaard, 1980). A model correlation function was chosen to fit the observed space and time coherences for each wavenumber and (D3) used to compute M for the given array geometry. Here M ranged from 23, for clockwise wavenumber 1, to 58, the number of profiles, for the spatially incoherent high wavenumbers. Eq. D3 was used, e.g., to compute the confidence limits for the vertical wavenumber spectrum (Fig. 6).

Degrees of freedom for the horizontal wavenumber spectra (Figs. 7, 8) were computed by distributing the total degrees of freedom for each wavenumber band M_β equally among the m energy estimates. The correlation function $C(\beta, r^*)$ was averaged over several vertical wavenumber bands to increase the total degrees of freedom. The correlation functions for each wavenumber scale more closely with r^* than Δr , corresponding to similar frequency rather than horizontal wavenumber spectra. Thus $C(\beta, r^*)$ rather than $C(\beta, \Delta r)$ was averaged. The additional degrees of freedom due to this vertical wavenumber band averaging are estimated following Persson (1974) as a factor of $B = 1.75$ for two bands and 2.48 for three bands. If the energy in the bands is unequal, the degrees of freedom are reduced by a factor A computed using (D2). The degrees of freedom are increased by the Bessel transform window because of its averaging in horizontal wavenumber; this gives a factor $K = 1.05$ for a 10% Tukey window (Fig. 7) and 1.5 for a Hanning window (Fig. 8) (Harris, 1978). Effectively, each estimate overlaps its neighbors by $K - 1$. When N'_b additional estimates of adjoining horizontal wavenumbers are band-averaged, this results in an increase in the degrees of freedom by roughly a factor $B' = (N'_b + K - 1)/K$.

The number of degrees of freedom for each spectral estimate is then

$$\frac{\text{EDOF}}{\text{estimate}} = 2M_\beta A B B' \frac{K}{m}, \quad (\text{D4})$$

which is used to compute the chi-squared 95% confidence limits in Figs. 7 and 8.

Given energies E_1 and E_2 , confidence limits on the fractional contributions $R_1 = E_1/(E_1 + E_2)$ and $R_2 = E_2/(E_1 + E_2)$ are computed by assuming E_1 and E_2 to be χ^2 distributed with ν_1 and ν_2 degrees of freedom. Using (D1) and assuming small errors, the variance of R_1 can be written

$$\text{var}[R_1] = \left[\frac{2(\nu_1 + \nu_2)}{\nu_1 \nu_2} \right]^{1/2} R_1(1 - R_1). \quad (\text{D5})$$

The 95% confidence limits are taken as $R_1 \pm 2 \times [\text{var}(R_1)]^{1/2}$.

REFERENCES

- Blackman, R. B., and J. W. Tukey, 1958: *The Measurement of Power Spectra from the Point of View of Communications Engineering*. Dover, 190 pp.
- Briscoe, M. G., 1977: Gaussianity of internal waves. *J. Geophys. Res.*, **82**, 2117-2126.
- D'Asaro, E. A., 1983: Wind forced internal waves in the North Pacific and Sargasso Sea. Submitted to *J. Phys. Oceanogr.*
- Fofonoff, N. P., 1969: Spectral characteristics of internal waves in the ocean. *Deep-Sea Res.*, **16**(Suppl.), 59-71.
- Fu, L. L., 1981: Observations and models of inertial waves in the deep ocean. *Rev. Geophys. Space Phys.*, **1a**, 141-197.
- Garratt, J. R., 1977: Review of drag coefficients over oceans and continents. *Mon. Wea. Rev.*, **105**, 915-929.
- Garrett, C. J. R., and W. Munk, 1972: Space-time scales of internal waves. *Geophys. Fluid Dyn.*, **3**, 225-264.
- , and —, 1979: Internal waves in the ocean. *Annual Review of Fluid Mechanics*, Vol. 11, 339-369.
- Gregg, M. C., and M. G. Briscoe, 1979: Internal waves, finestructure, microstructure and mixing in the ocean. *Rev. Geophys. Space Phys.*, **17**, 1524-1548.
- , and T. B. Sanford, 1980: Signatures of mixing from the Bermuda Slope, the Sargasso Sea and the Gulf Stream. *J. Phys. Oceanogr.*, **10**, 105-127.
- Hamilton, G. D., 1980: NOAA data buoy office programs. *Bull. Amer. Meteor. Soc.*, **61**, 1012-1017.
- Harris, F. J., 1978: On the use of windows for harmonic analysis with the discrete fast Fourier transform. *Proc. IEEE*, **66**, 51-83.
- Hildebrand, F. B., 1976: *Advanced Calculus for Applications*, 2nd ed., Prentice-Hall, 816 pp.
- Käse, R. H., and R. A. Clark, 1978: High-frequency internal waves in the upper thermocline during GATE. *Deep-Sea Res.*, **25**, 815-825.
- Kang, Y. Q., and L. Magaard, 1980: Annual baroclinic Rossby waves in the central North Pacific. *J. Phys. Oceanogr.*, **10**, 1159-1167.
- LeBlond, P. H., and L. A. Mysak, 1978: *Waves in the Ocean*. Elsevier Scientific, 602 pp.
- Leaman, K. D., 1976: Observations on the vertical polarization and energy flux of near-inertial waves. *J. Phys. Oceanogr.*, **6**, 894-908.
- , and T. B. Sanford, 1975: Vertical energy propagation of inertial waves: A vector analysis of velocity profiles. *J. Geophys. Res.*, **80**, 1975-1978.
- McComas, C. H., and P. Müller, 1981: Time scales of interactions among oceanic internal waves. *J. Phys. Oceanogr.*, **11**, 139-147.

- Müller, P., and G. Siedler, 1976: Consistency relations for internal waves. *Deep-Sea Res.*, **23**, 613–628.
- , D. J. Olbers and J. Willebrand, 1978: The IWEX spectrum. *J. Geophys. Res.*, **83**, 479–500.
- Perkins, H., 1972: Inertial oscillations in the Mediterranean. *Deep-Sea Res.*, **19**, 289–296.
- , 1980: Oceanic environmental background observations in the Sargasso Sea during September 1979. Tech. Note 58, Naval Ocean Research and Development Activity, NSTL Station, MS, 279 pp.
- Persson, J., 1974: Variability and covariability of modified spectral estimators. *IEEE Trans. Acoustics, Speech and Signal Processing*, **ASSP-22**, 158–160.
- Pollard, R. T., 1969: On the generation by winds of inertial waves in the ocean. *Deep-Sea Res.*, **17**, 795–812.
- , 1980: Properties of near-surface inertial oscillations. *J. Phys. Oceanogr.*, **10**, 385–398.
- , and R. C. Millard, 1970: Comparison between observed and simulated wind-generated inertial oscillations. *Deep-Sea Res.*, **17**, 813–821.
- Ruddick, B. R., 1977: Observations of interaction between the internal wave field and low frequency flows in the North Atlantic, Ph.D. thesis, WHOI, Woods Hole, MA, 334 pp.
- Sanford, T. B., 1975: Observations of the vertical structure of internal waves. *J. Geophys. Res.*, **80**, 3861–3871.
- , R. G. Drever and J. H. Dunlap, 1978: A velocity profiler based on the principles of electromagnetic induction. *Deep-Sea Res.*, **25**, 183–200.
- , —, and E. A. D'Asaro, 1982: Design, operation and performance of an Expendable Temperature and Velocity Profiler (XTVP). APL-UW 8110, Applied Physics Laboratory, University of Washington, 164 pp.
- Seaver, G. A., and S. Kuleshov, 1982: Experimental and analytical error of the expendable bathythermograph. *J. Phys. Oceanogr.*, **12**, 592–600.
- Webster, F., 1968: Observations of inertial period motions in the deep sea. *Rev. Geophys.*, **4**, 473–490.
- Welch, P. D., 1967: The use of fast Fourier transform for the estimation of power spectra: A method based on time averaging over short, modified periodograms. *IEEE Trans. Audio Electro-Acoust.*, **AU-15**, 70–73.
- Weller, R. A., 1982: The relation of near-inertial motions observed in the mixed layer during the JASIN (1978) experiment to the local wind stress and to the quasi-geostrophic flow field. *J. Phys. Oceanogr.*, **12**, 1122–1136.
- Willebrand, J., 1978: Temporal and spatial scales of the wind field over the North Pacific and North Atlantic. *J. Phys. Oceanogr.*, **8**, 1080–1094.
- Zetler, B., W. Munk, H. Mofjeld, W. Brown and F. Dormer, 1975: MODE tides. *J. Phys. Oceanogr.*, **5**, 430–441.